Additive Manufacturing 36 (2020) 101671

Contents lists available at ScienceDirect

Additive Manufacturing

journal homepage: www.elsevier.com/locate/addma

Research Paper

Systematic analysis of the mechanical anisotropy of fibre-reinforced polymer specimens produced by laser sintering

A. Khudiakova [a], M. Berer [a,*], S. Niedermair [b,c], B. Plank [d,e], E. Truszkiewicz [a], G. Meier [a], H. Stepanovsky [b,f], M. Wolfahrt [a], G. Pinter [g], J. Lackner [h]

[a] Polymer Competence Center Leoben GmbH, Roseggerstraße 12, 8700 Leoben, Austria
[b] Bernstein Innovation GmbH, Froschberg 3, 4020 Linz, Austria
[c] NBG Dimensions, Zweiländerstraße 1, 3950 Gmünd, Austria
[d] University of Applied Sciences Upper Austria, Stelzhamerstraße 23, 4600 Wels, Austria
[e] University of Augsburg, Universitätsstraße 2, 86159 Augsburg, Germany
[f] NEMETON Innovation GmbH, Jetzleser Straße 17, 3902 Vitis, Austria
[g] Institute of Materials Science and Testing of Polymers, Montanuniversitaet Leoben, Otto Gloeckel-Straße 2, 8700 Leoben, Austria
[h] JOANNEUM RESEARCH Forschungsgesellschaft mbH, Leobner Straße 94, 8712 Niklasdorf, Austria

ARTICLE INFO

Keywords:
Selective laser sintering
Polyamide
Short carbon fibre composites
Fibre orientation
X-ray computed tomography

ABSTRACT

Selective laser sintering (SLS) is an additive manufacturing process which nowadays receives abundant attention from industry sectors. However, the number of materials which can be processed by SLS is still very limited and requires further research. The present work aims to contribute to this topic by investigating the mechanical properties of neat and short carbon fibre reinforced polyamide 1212 processed by SLS. The specimens were built in different spatial alignments to obtain ample details on the tensile behaviour. The detailed examinations of the fractured specimens were performed by means of optical microscopy, scanning electron microscopy and X-ray computed tomography. The comprehensive analysis revealed that most of the fibres (85 – 95%) were oriented in the plane of the powder layer and here, the majority along the direction of the moving roller coater, which distributes the powder on the powder bed of the SLS machine. It was shown that this effect has a direct impact on the strength and stiffness of the printed tensile bars and thus on the mechanical behaviour of SLS printed parts. Furthermore, the analysis results indicate the possibility to control this mechanical anisotropy through a systematic alignment of the components in the powder cake.

1. Introduction

Selective laser sintering (SLS) is one of the oldest techniques in the modern field of additive manufacturing. Its invention officially took place at the University of Texas and it dates back to the 1980 s [1]. After its invention, it took many years until the first commercially available SLS machines were finally on the market. Subsequently, until 2014, this market was dominated by the companies 3D Systems (3D Systems Corporation, Rock Hill, South Carolina) and EOS (EOS GmbH – Electro Optical Systems, Krailling, Germany), which were holding the key patents for this technique at that time [2]. Since these patents expired, many new machine producers have appeared on the market, making it much more inhomogeneous now. The broader competition on the market has led to big progress steps in machine technology in recent years. As a result, SLS is not limited to the production of prototypes anymore, but is also accepted in the serial production of small and medium lots.

Compared to conventional polymer processing techniques, such as extrusion and injection moulding, SLS is still rather limited concerning the materials available for the process. However, since 2014, the boosted machine progress has caused a big number of newly developed polymer powders to be released. Aside from the extension of the SLS technique to new polymers [3–9], the compounding and reinforcement of the neat polymers, especially polyamide 12, are also in the focus for this. The modification of the powders aims at different material aspects, for instance improvement in the tribological behaviour with molybdenum disulfide (MoS_2), modification of thermal and electrical conductivity and mechanical properties using carbon nanotubes, carbon black,

* Corresponding author.
E-mail address: Michael.Berer@pccl.at (M. Berer).

https://doi.org/10.1016/j.addma.2020.101671
Received 23 June 2020; Received in revised form 17 September 2020; Accepted 14 October 2020
Available online 17 October 2020

etc. [10–16], and improvement in the mechanical behaviour using glass beads and carbon fibres [17–23].

The mechanical reinforcement of a polyamide powder using carbon fibres was also a topic in the present research. While other research in this field focused especially on the production of the composite [10,18,20,21,24], in this study, it was simply produced by directly mixing polyamide powder with carbon fibres, both of which are commercial products. Adding the stiff fibres to the neat powder leads to the anisotropy of mechanical properties of the output part [19,23,25,26]. Few research works have found that the fibres tend to lie along the moving direction of a roller or a rake used to distribute the powder over the printing platform [19,23,26]. However, the fibre alignment and its influence on the mechanical performance were not characterised in details and require further analysis. Therefore, the clear focus in this research was to examine the influence of the SLS process on the resulting fibre orientation and, hence, the mechanical properties of the SLS printed components. For this, differently aligned dog-bone shaped tensile specimens were SLS printed using neat and reinforced powder. The mechanical performance of the specimens was characterised using tensile tests. Additionally, powder and part morphology were studied using microscopy and X-ray computed tomography.

2. Experimental

2.1. Materials

Neat and reinforced specimens were produced out of the polyamide 1212 based nylon powder FS 3300PA provided by Farsoon (Farsoon Europe GmbH, Germany) [27]. For the reinforced specimens, the powder resin was directly mixed with 12 wt% of Sigrafil short carbon fibres (SGL Carbon, Germany) [28] in a barrel mixer. According to the supplier, the average fibre length and diameter was about 80 μm and 7 μm, respectively. The fibre content of 12 wt% was chosen on the grounds of preliminary tests with different fibre mass contents and literature research [22]. The basic material parameters of the components are presented in Table 1.

2.2. Specimen manufacturing

The powder mixture prepared was sintered in an sPro 60 SLS printer (3D System Corporation, SC, USA), which was modified by LSS Laser Sinter Service GmbH (Germany) in order to improve the uniformity and stability of the building process. Since adding of carbon fibres to the neat powder changes its absorption of the laser heat [11,23], the process parameters were optimised for neat and reinforced specimens separately. The layer thickness of 0.1 mm was used for both, neat and reinforced specimens. The specimens had a dog-bone shape with the type-A dimensions from ISO 527 [29]. Nylon powder, distributed with a roller moving in the *x*-direction, was sintered layer by layer till the specimens were completed (Fig. 1).

The specimens were printed in different directions to investigate the influence of the alignment in the powder cake on the mechanical properties. The specimens formed three fans in the *xy*-, *xz*- and *yz*-planes with printing orientations from 0° to 90° with steps of 22.5° (Fig. 1a). Three specimens were printed for every spatial position. For the sake of the test repeatability, an additional specimen set was printed in the other corner of the chamber with the same specimen alignment (Fig. 1b). Hereafter, the specimens are denominated according to their coordinate plane angle, where the coordinate plane is either *xy*, *xz*, or *yz*, and the angle is either 0°, 22.5°, 45°, 67.5° or 90°. For example, *xz*-45° refers to a specimen printed in the *xz*-plane at 45°, where *x* corresponds to the moving direction of the roller distributing the powder and *z* is the vertical axis normal to the printing platform. The same building configuration was used for neat polyamide specimens, which were printed for reference purposes. Prior to testing, all specimens were dried at 80 °C for at least 12 days in a vacuum drying oven to eliminate the moisture content.

Table 1.
Properties of components used for the powder mixture.

	FS 3300PA [27]	Carbon fibres [28]
Melt temperature	183 °C	
Tensile strength	46 MPa	4 GPa
Tensile modulus	1602 MPa	240 GPa
Strain at break	36%	1.7%

2.3. Tensile tests

Tensile tests were performed on the universal testing machine Zwick Z250 (Zwick GmbH & Co. KG, Germany), equipped with a load cell of 10 kN. The tests were carried out in accordance with ISO 527 [29]. The specimens were tested at room temperature with an initial pre-load of 0.1 MPa and a cross-head speed of 1 mm/min for the modulus determination regime (0.05–0.25%) and then at 50 mm/min till the final rupture. Specimens were compared in terms of maximum tensile strength σ, Young's modulus E and strain at break ε_b. Young's modulus was calculated according to Eq. 1 [29]. Three specimens were tested for every spatial position of both specimen fans.

$$E = \frac{\Delta\sigma}{\Delta\varepsilon} \tag{1}$$

where $\Delta\varepsilon$ refers to the difference between two longitudinal strain points and $\Delta\sigma$ to the difference in applied tensile stress between these two strain points. The values were evaluated with $\Delta\varepsilon$ of 0.2% according to ISO 527 [29].

2.4. X-ray computed tomography

The high-resolution X-ray computed tomography (μCT) was performed using the μCT device Nanotom 180 NF (GE Phoenix x-ray, Wunstorf, Germany), equipped with a 180 kV nanofocus X-ray tube. The overall scans with an edge length of a volumetric pixel (voxel size) of $(4.5\ \mu m)^3$ were carried out at the tube voltage, the integration time and the number of projections of 60 kV, 500 ms and 1700, respectively. For full fibre characterisation, detailed scans with the voxel size of $(1.4\ \mu m)^3$ were performed. To achieve a small focal spot size, the maximum target power of the electron beam in the X-ray tube is limited, so the integration time was increased to 900 ms to achieve proper saturation of the detector image brightness. The parameters used yielded scan times of 177 and 233 min for the overall and detailed examinations, respectively. As a target material, molybdenum on a beryllium window was used for all scans.

To reach a resolution of $(1.4\ \mu m)^3$ voxel size, small μCT samples of $2\times2\text{x}10\ mm^3$ were cut out near the specimen shoulders, as shown in Fig. 2. They were aligned inside the X-ray device in the same way for every specimen. The samples were taken from the fractured specimen parts after tensile testing. The μCT analysis was carried out for the reinforced specimens printed in the directions *xy*-0°, *xy*-45°, *xy*-90°, *xz*-45°, *xz*-90° and *yz*-45°. One sample cut out of one specimen was examined per printing direction. The μCT data analysis was performed using the commercially available software tool VG Studio MAX 3.3 (Volume Graphics, Germany) and the in-house developed software iAnalyse [30,31], for which most implementations are also available in the open-source software open_iA [32]. Two software tools were used in order to compare and verify the results regarding the mean orientation of the fibres in the reinforced specimens. Using only iAnalysis would have led to a potential underestimation of the number of fibres in a certain direction, since the fibres shorter than 50 μm were not examined. VG Studio MAX 3.3 uses a grey value based analysis method, delivering the orientation of all individual voxels within a certain grey value range,

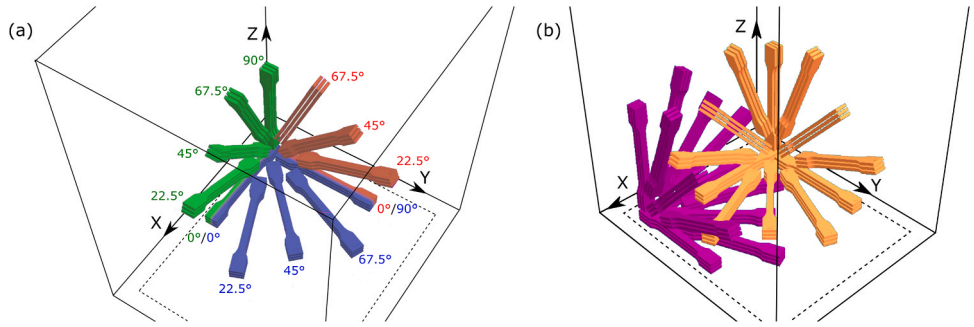

Fig. 1. Graphic representation of (a) the spatial alignment of the three fans of tensile bars in the build chamber (a) and the position of the additional specimen set (b). The roller spread the powder in the *x*-direction. (For interpretation of the references to colour in this figure legend, the reader is referred to the web version of this article.)

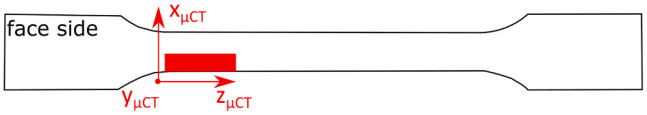

Fig. 2. Schematic illustration of a μCT sample cut out of the specimen produced by SLS. The coordinate system ($x_{\mu CT}$,$y_{\mu CT}$, $z_{\mu CT}$) marked in red corresponds to the spatial alignments in the X-ray device, where the $x_{\mu CT}y_{\mu CT}$ plane corresponds to the rotation stage and $z_{\mu CT}$ to the rotation axis of the X-ray device. (For interpretation of the references to colour in this figure legend, the reader is referred to the web version of this article.)

but has not the possibility to extract additional information such as the length of individual fibres.

2.5. Optical analysis

Optical analyses were used to investigate the impact of the fibres on the mechanical behaviour of the material. After the tensile tests, the face (broad surface), side (thin surface) and fracture surfaces of the samples were examined by means of optical microscopy and scanning electron microscopy (SEM). The micrographs were made with the optical microscope Olympus SZX12 (Olympus Corporation, Japan). The SEM examination was performed with the Tescan Vega II electron microscope (Tescan Orsay Holding, a.s., Brno, Czech Republic). Prior to the examination, the specimens were coated with gold to reduce the surface charging. The accelerating voltage for the electrons was set up to 5 kV; the working distance used was 8–16 mm. In addition, the morphology of the filled powder was characterised by SEM.

3. Results and discussion

The two specimen sets built in the different corners of the building chamber showed similar results within the corresponding angle alignments. This reveals that for the area examined, the mechanical properties were not significantly influenced by the position in the powder cake during production. Therefore, the results were combined and are presented for six specimens (instead of two times three) of every printing direction.

3.1. X-ray computed tomography of the reinforced specimens

The μCT analysis was performed to determine the void content as well as the length, number and orientation of the fibres in the *xy*-0°, *xy*-45°, *xy*-90°, *xz*-45°, *xz*-90° and *yz*-45° carbon fibre (CF) reinforced specimens. The alignment of the specimens inside the X-ray device during the overall scans and with respect to the coordinate axes is shown in Fig. 3. The detailed scans with the voxel size of $(1.4\ \mu m)^3$ were performed in the mid-part of every sample.

For the porosity characterisation, voids in the *xy*-0° sample were evaluated semi-automatically using the voxel size of $(1.4\ \mu m)^3$. This scan yielded the reference value for the 'proper' porosity obtained at high resolution of 4.00 vol.-% (Fig. 4a,b), which was used to determine the threshold value from the grey-level intensity histogram. According to the positions of the air – and material peak, a ratio of 42% (ISO42) was determined as an optimum threshold value [33–35]. The threshold defined was used for the automated segmentation of voids in the *xy*-0° sample scanned at lower resolution using the voxel size of $(4.5\ \mu m)^3$. This led to the porosity content of 4.01 vol% (Fig. 4d,e). Application of the automated segmentation of voids at lower resolution to the other five samples revealed porosity content of about 4.2 vol% as an average of all six samples investigated by μCT (Table 2).

The fibre characterisation was performed following the concept of medial axis extraction (MAE) implemented by using template matching (TM) [36,37]. According to the TM approach, the fibres evaluated are allowed to be curved and are considered to have circular cross sections of the same diameter. A voxel template generated had a spherical shape and the same diameter and grey value as the carbon fibres. The template was correlated with individual fibres in the scanned samples to define the fibre orientations. The ideal template to correlate with straight fibres

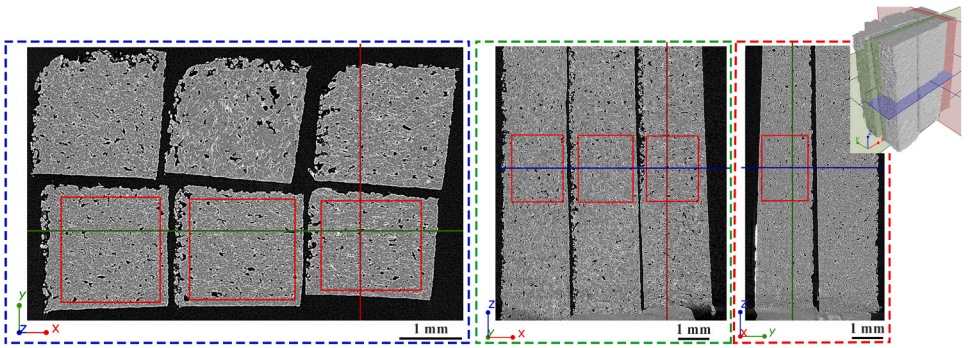

Fig. 3. Orthogonal μCT slice images through the individual samples scanned at $(4.5\ \mu m)^3$ voxel size: top (a), front (b), right (c) and 3D rendering (d). Red areas identify the representative region of interest for porosity evaluation and detailed high resolution scans for full fibre characterizations. Samples *xy*-0°, *xy*-45°, *xy*-90° are represented in the bottom row and *yz*-45°, *xz*-45°, *xz*-90° are represented in the top row in (a). (For interpretation of the references to colour in this figure legend, the reader is referred to the web version of this article.)

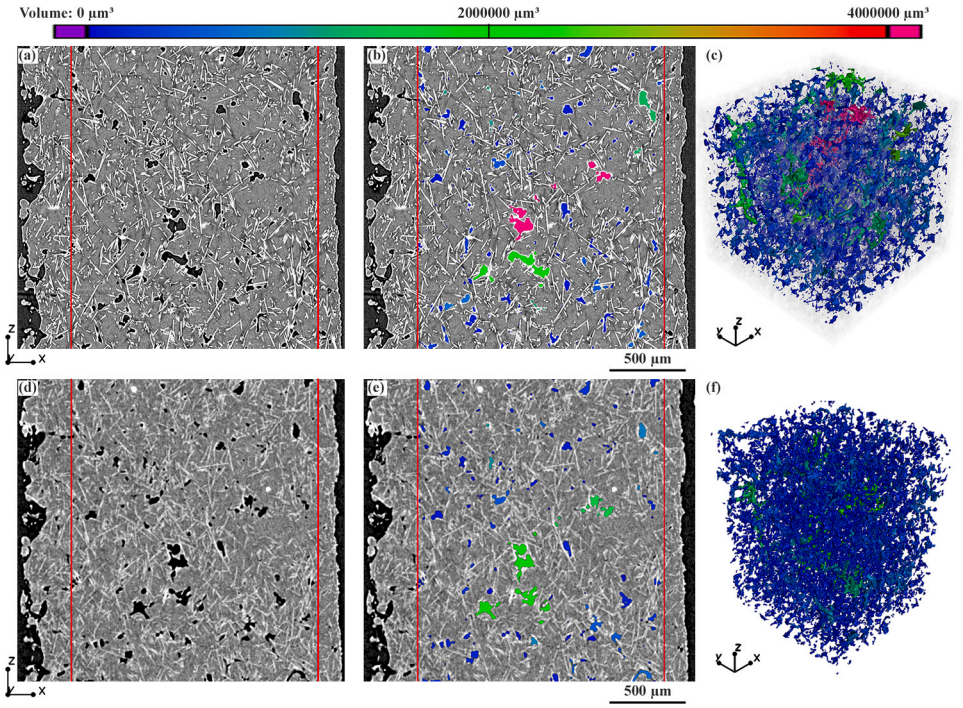

Fig. 4. A high resolution scan of the *xy*-0° sample scanned at $(1.4\ \mu m)^3$ voxel size (a), which was used for a semi-automated determination of the reference porosity of 4.00 vol% (b). The same region of the sample scanned at $(4.5\ \mu m)^3$ voxel size (d). An automated pore segmentation with the ISO42 threshold, which yielded a void content of 4.01 vol% (e). 3D rendering of the segmented voids is demonstrated in (c) and (f). (For interpretation of the references to colour in this figure legend, the reader is referred to the web version of this article.)

Table 2.
Void volume content and fibre lengths obtained using the X-ray computed tomography.

	xy-0°	*xy*-45°	*xy*-90°	*xz*-45°	*xz*-90°	*yz*-45°
Void volume content, vol%	4.01	4.05	4.15	4.37	4.53	4.09
Weighted average fibre length, µm	101.9	100.7	101.6	101.4	96.8	101.4
Average fibre length, µm	87.0	86.2	86.8	86.7	83.5	86.6
Total number of evaluated fibres	1,20,200	1,20,630	84,080	90,575	78,410	1,02,615
Maximum fibre length, µm	438.3	444.4	417.5	593.2	502.5	469.7

would be a cylinder. However, the spherical shape was chosen over cylindrical based on the previous research [37] and in order to save calculation time. For the initial binarization of every individual fibre, the ISO270 threshold was determined from the grey level histogram empirically and applied to every individual dataset. Fig. 5a,c shows the extracted medial axes of every individual carbon fibre in random colours depending on the individual fibre ID. For better visualisation of the individual fibres in 2D, which are usually not aligned completely within one slice plane, a thickness of 25 µm was used for the maximum intensity image mode shown in Fig. 5a. A length threshold of 50 µm was chosen for the fibre evaluation to avoid miss-segmentations near voids. All fibres shorter than 50 µm were not taken into consideration for further quantitative evaluations. The start and end points obtained for every individual fibre were used for the calculations of the average fibre length and the weighted average fibre length according to ISO 22314 [38] as well as for the determination of the fibre orientation in the 3D volume (Table 2, Fig. 5). It was shown that most of the fibres had a weighted average length of about 101 µm and an average fibre length of 86 µm in all examined samples (Table 2). It is worthwhile noting that the fibre lengths obtained are rough guide values, because the fibres shorter than 50 µm were not taken into account to avoid possible miss-segmentations of phase contrast edge effects along every void occurring in the high-resolution µCT [39]. For a small minority of fibre interacts, the algorithm was not able to track the entire fibre length, because of virtual fibre breakage. Therefore, the real average length is expected to be shorter. This finding is in good agreement with the data sheet from the supplier, where an average fibre length of 80 µm is stated [28]. The maximum fibre length evaluated by means of µCT was 593 µm (Table 2). The complete fibre length distribution of the relative number of fibres versus the length is illustrated in Fig. 6 for different building directions.

Further analysis revealed a significant difference in the fibre orientation, which supports the discussions below (Fig. 7). In the *xy*-0° sample, more than 50% of the fibres were oriented along the $z_{\mu CT}$-axis. In the *xy*-90° sample, most of the fibres were aligned along the $x_{\mu CT}$-axis and, in the *xz*-90°, along the $y_{\mu CT}$-axis. In all cases, the preferable fibre orientation corresponded to the direction of the roller inside the SLS machine. These results were shown by both software tools, iAnalyse (Fig. 7a) and VG (Fig. 7b), for the extremely high numbers of fibres evaluated (Table 2). These findings offer overwhelming evidence for the existence of a preferable fibre orientation in the specimens produced in the SLS process. Moreover, there is a good correlation with the roller direction and the layer structure typical for SLS: 50 – 60% of the fibre orientation is in-plane of the powder layer along the roller direction (*x*-axis), 30 – 40% perpendicular to it but also in-plane of the powder layer (along the *y* -axis) and another 5 – 15% is oriented out-of-plane of the powder layer (along the *z*-axis).

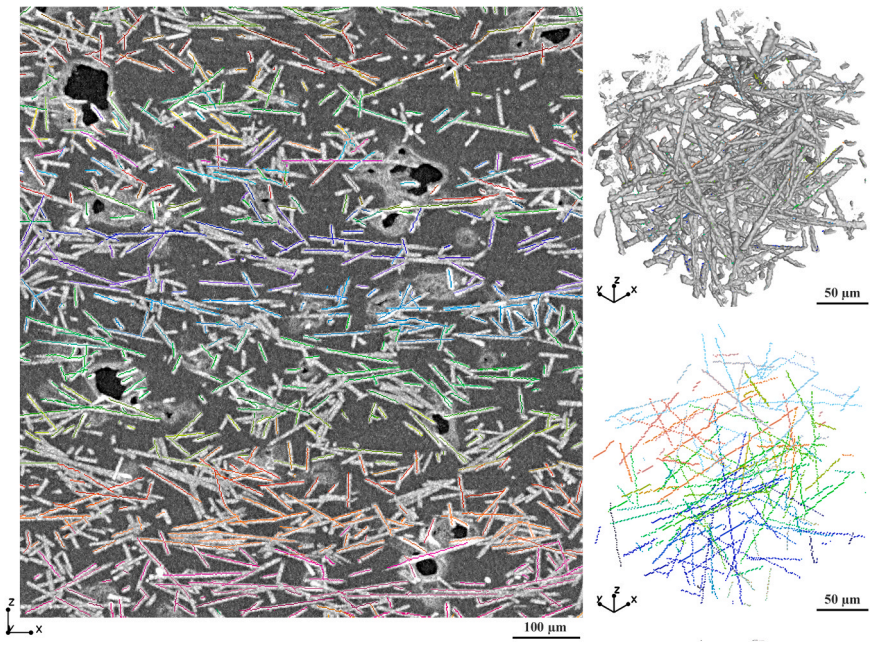

Fig. 5. Visualisation of the extracted medial axes of every individual fibre for the *yz*-45° sample scanned at (1.4 µm)^3 voxel size (a). 3D rendering of a small cut-out of the dataset of individual fibres (b) and their medial axes extractions (c). (For interpretation of the references to colour in this figure legend, the reader is referred to the web version of this article.)

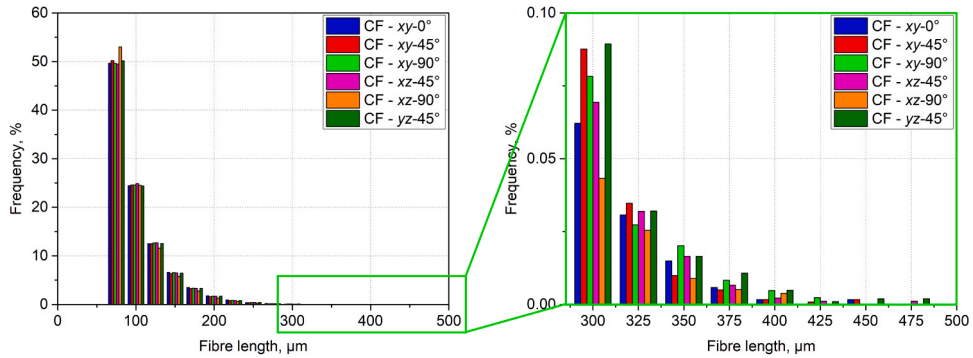

Fig. 6. Fibre length distribution in the CF reinforced specimens. (For interpretation of the references to colour in this figure legend, the reader is referred to the web version of this article.)

3.2. Tensile test results

3.2.1. Tensile tests of the neat specimens

The representative stress-strain curves of the neat specimens are illustrated in Fig. 8. The results of the tensile tests of the neat specimens are summarised in Table 3 and depicted in Fig. 9. The tensile strengths and Young's moduli obtained for the specimens from the *xy*, *xz* and *yz*-planes showed nearly the same magnitudes for every printing direction - about 43 ± 4 MPa and 1803 ± 47 MPa, respectively. However, the more vertical printing directions like *xz*-67.5, *xz*-90°, etc. showed a bit lower values of tensile strength and Young's modulus in comparison with the other specimens. This can be explained by the fact that the loading force was applied (nearly) transverse to the layer interfaces created due to the layer-wise manufacturing process [40]. The results obtained are in good agreement with regard to the material data provided by the supplier [27] (Table 1). In addition, the present results obtained for PA1212 are consistent with other research works [40,41], which have investigated SLS specimens out of PA12, indicating the similarity of these two materials. Similar values for the neat specimens built in different directions, apart from the more vulnerable vertical directions, means low mechanical anisotropy [42] and further indicates well selected processing parameters. However, the strain at break, which is generally much more sensitive to the process parameters, in particular to the thermal history, than tensile strength or Young's modulus [40], did not show such a uniform behaviour. Instead, there was distinct scatter within the different specimen alignments and a strong deviation between them. All together the values varied from a minimum value of 5% for *xz*-90° to a maximum value of 13.5% for *xy*-67.5°. The high scatter level within the same specimen alignments is attributed to variations of the porosity and the quality of the layer to layer fusion from specimen to specimen. Regarding the deviation between the different alignments, no unambiguous tendency can be deduced from the values in Table 3 and Fig. 9.

3.2.2. Tensile tests of the reinforced specimens

The representative stress-strain curves of the carbon fibre reinforced polyamide specimens are shown in Fig. 8b. The corresponding tensile test results are presented in Table 3 and depicted in Fig. 9 and Fig. 10. As expected, the experiments demonstrated the strengthening and stiffening of the matrix reinforced with carbon fibres [18,21,23]. The tensile strength σ was increased by almost a factor of two for the *xy*-0° specimens and by a factor of 1.4 for the *xy*-90° specimens in comparison with

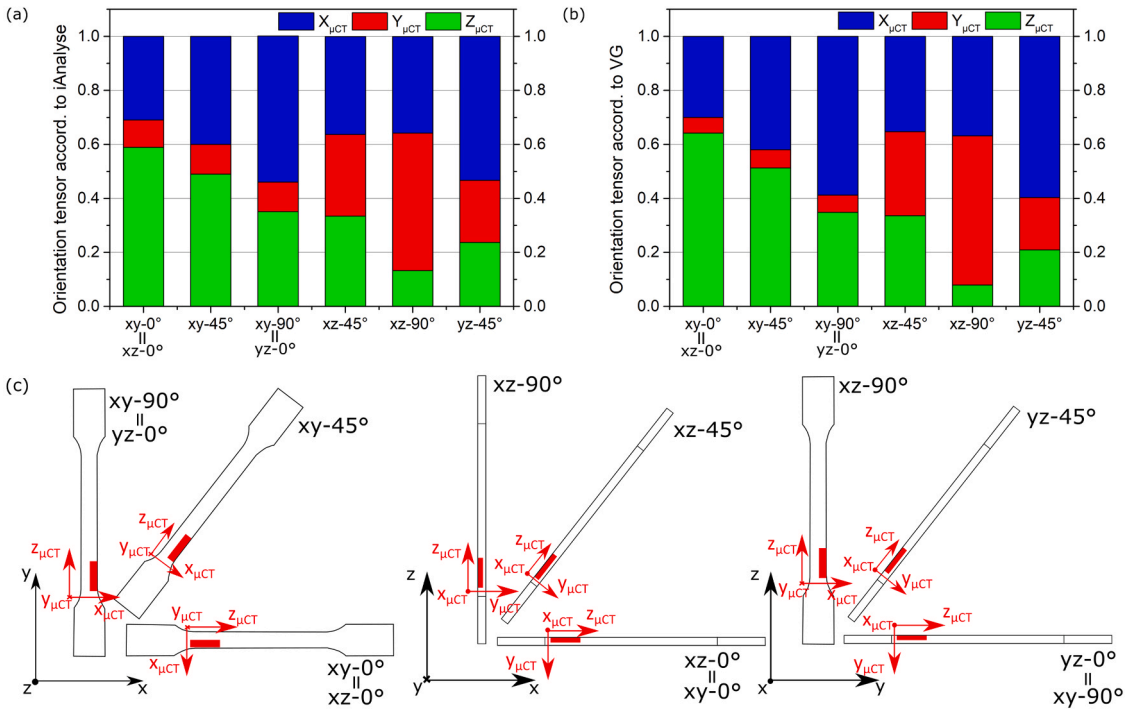

Fig. 7. Distributions of the fibre orientations in the μCT samples evaluated by the iAnalysis (a) and VG (b) software tools, and a schematic representation of the μCT samples (red rectangles) cut out of the SLS specimens (c). ($x_{\mu CT}$, $y_{\mu CT}$, $z_{\mu CT}$) marked in red corresponds to the coordinate system of the X-ray device, where the $x_{\mu CT}y_{\mu CT}$-plane is a plane of the rotation stage and $z_{\mu CT}$ is the rotation axis. (x, y, z) marked in black corresponds to the coordinate system of the SLS machine, where x is the direction of the powder distributing roller. (For interpretation of the references to colour in this figure legend, the reader is referred to the web version of this article.)

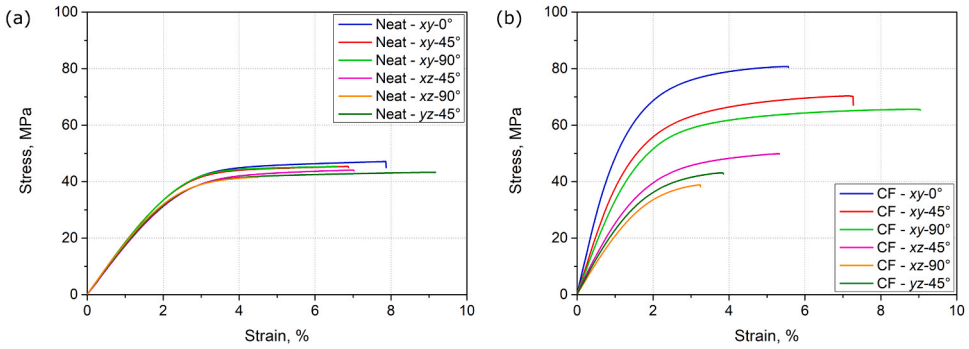

Fig. 8. Representative stress-strain curves of the neat (a) and CF reinforced (b) specimens. (For interpretation of the references to colour in this figure legend, the reader is referred to the web version of this article.)

the neat specimens. Regarding the *xz* and *yz* specimens, the carbon fibres made the specimen stronger for 0° and 22.5°, but starting from 45° the reinforcing effect started to disappear. This is well depicted as overlapping of the dashed green and red lines with the corresponding tendencies of the neat specimens in Fig. 10a. The biggest influence of the carbon fibres on Young's modulus E was achieved for the *xy* specimens. It was almost three times bigger for the *xy*-0° specimens reinforced with carbon fibres than for the neat specimens. This difference gradually decreased to a factor of two with the angle increase from 0° to 90°. The strain at break ε_b of the CF reinforced specimens showed less scattering in comparison with the results of the neat specimens. The *xy* specimens yielded the highest ε_b of 6–9%, followed by 3–6% for the *xz*- and 3–5% for the *yz* specimens.

For the CF reinforced specimens built in different directions, the highest σ of about 80 MPa and E of about 5600 MPa were achieved by the specimens printed along the *x*-axis. These results are consistent with [18], where σ of 72 MPa and E of 5500 MPa were reported for PA12 specimens reinforced with 30%wt carbon fibres. With the angle increase within the *xy*-plane from 0° to 90°, the tensile strength and the Young's modulus gradually decreased to 65 and 3500 MPa, respectively. The tensile strength and the Young's modulus of specimens in the *xz*- and *yz*-planes progressively reduced from the horizontally to the vertically oriented specimens. The specimens printed vertically along the *z*-axis yielded the lowest σ and E among all specimens of 40 MPa and 2400 MPa, respectively.

These findings can be explained by the preferable fibre orientations in the specimens shown above, which influence the mechanical properties. As illustrated in Fig. 7, the roller orients the fibres along its moving direction (*x*-axis), when distributing a new layer of powder on the building platform. This effect was also reported in [19], where it was shown that most of the fibres were oriented in the *x*-direction of the build chamber. As a consequence, the specimens with the fibres oriented along the loading direction are able to bear higher stresses than those with the fibres oriented out of the loading plane [43]. That way, for

Table 3
Results of the tensile tests: the strength, Young's modulus and strain at break of the neat and carbon fibre (CF) reinforced specimens built in different directions.

	XY		XZ		YZ	
	Neat	**With CF**	**Neat**	**With CF**	**Neat**	**With CF**
***σ*, MPa**						
0°	47.2 ± 1.3[a]	80.8 ± 0.5[a]	47.2 ± 1.3[a]	80.8 ± 0.5[a]	45.2 ± 1.5[b]	64.9 ± 0.7[b]
22.5°	46.2 ± 2.0	76.1 ± 1.7	44.6 ± 1.2	62.2 ± 3.6	45.8 ± 0.2	53.9 ± 1.5
45°	45.4 ± 0.9	70.7 ± 0.3	44.1 ± 0.7	50.2 ± 1.5	43.8 ± 0.3	43.6 ± 2.0
67.5°	46.1 ± 1.6	66.0 ± 0.6	41.4 ± 1.2	43.0 ± 3.5	41.8 ± 0.3	38.8 ± 2.6
90°	45.2 ± 1.5[b]	64.9 ± 0.7[b]	41.7 ± 0.6	39.4 ± 2.1	–	–
***E*, MPa**						
0°	1851 ± 14[a]	5644 ± 123[a]	1851 ± 14[a]	5644 ± 123[a]	1829 ± 36[b]	3616 ± 78[b]
22.5°	1863 ± 21	5104 ± 168	1806 ± 21	3871 ± 130	1809 ± 18	2917 ± 93
45°	1843 ± 19	4292 ± 185	1726 ± 28	2565 ± 96	1791 ± 25	2390 ± 66
67.5°	1854 ± 34	3731 ± 49	1741 ± 36	2301 ± 92	1756 ± 12	2213 ± 178
90°	1829 ± 36[b]	3616 ± 78[b]	1787 ± 45	2326 ± 77	–	–
ε_b, %						
0°	10.1 ± 5.3[a]	6.3 ± 0.5[a]	10.1 ± 5.3[a]	6.3 ± 0.5[a]	8.1 ± 6.6[b]	8.5 ± 0.5[b]
22.5°	9.6 ± 6.1	6.0 ± 0.8	7.0 ± 3.7	4.6 ± 1.4	13.0 ± 1.8	5.3 ± 0.7
45°	8.8 ± 5.9	8.0 ± 0.6	10.1 ± 2.0	5.9 ± 1.2	10.0 ± 1.8	3.8 ± 0.6
67.5°	13.5 ± 9.3	8.9 ± 0.4	5.6 ± 1.9	3.6 ± 1.0	6.4 ± 0.9	2.8 ± 0.4
90°	8.1 ± 6.6[b]	8.5 ± 0.5[b]	5.0 ± 0.9	2.8 ± 0.5	–	–

[a] XY-0° is identical to XZ-0°
[b] XY-90° is identical to YZ-0°

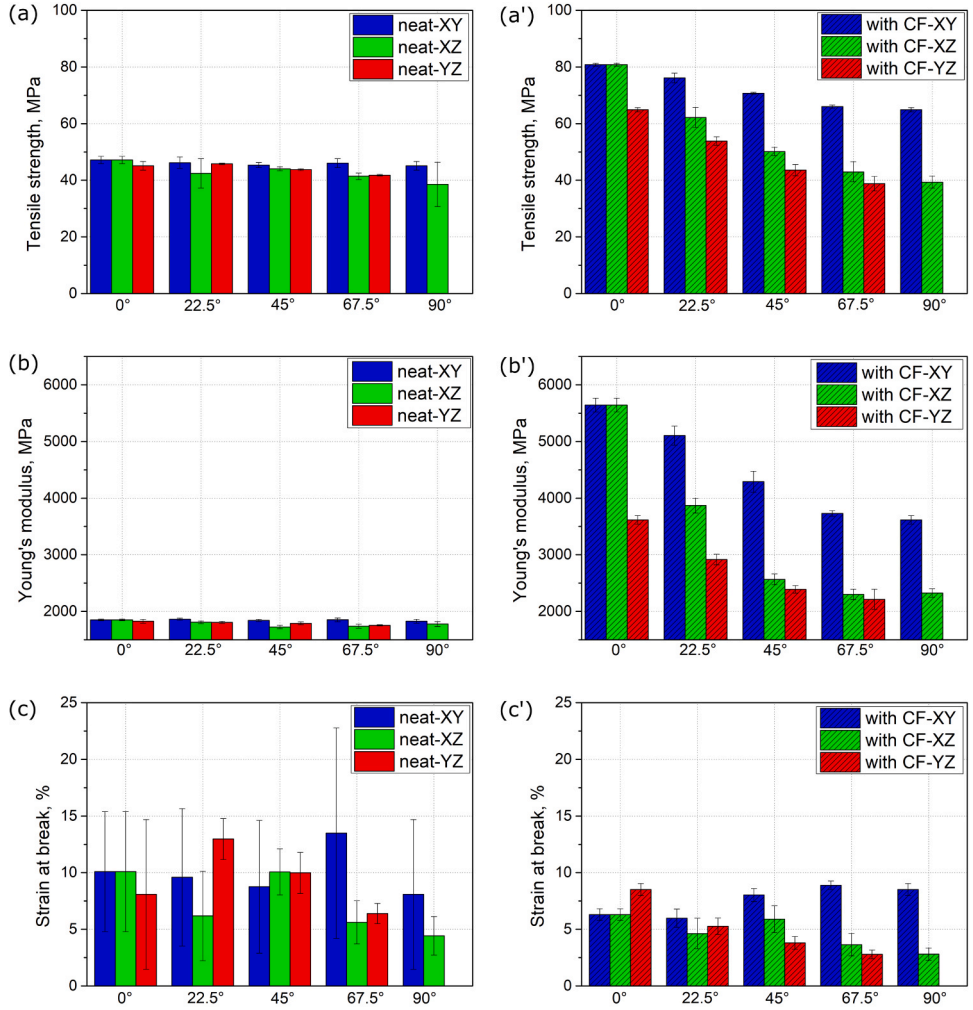

Fig. 9. Plots of the tensile strength, Young's modulus and strain at break obtained from the tensile tests of neat (a, b, c) and carbon fibre (CF) reinforced specimens (a′,b′,c′) manufactured in different building directions. The error bars represent the standard deviation from the corresponding average value. (For interpretation of the references to colour in this figure legend, the reader is referred to the web version of this article.)

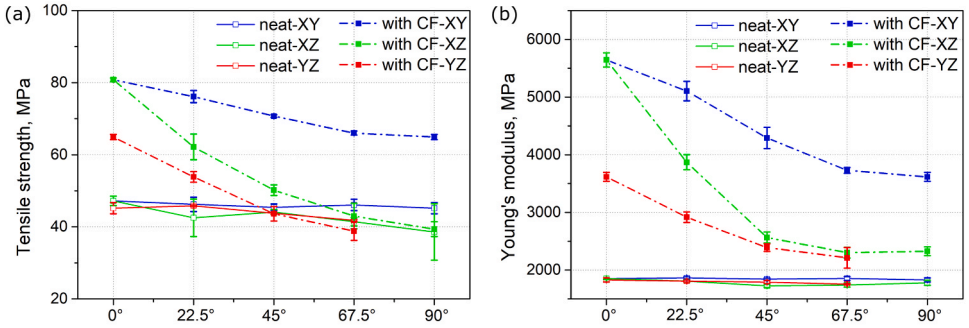

Fig. 10. Tendencies of the tensile strength (a) and Young's modulus (b) obtained for the neat and carbon fibre (CF) reinforced specimens. The error bars represent the standard deviation from the corresponding average value. (For interpretation of the references to colour in this figure legend, the reader is referred to the web version of this article.)

example, the *xy*-90° specimens were stronger than the *xz*-90° specimens, although they have the same preferable fibre orientation along the *x*-direction. However, along the tensile loading direction, which is the *y*-direction for the *xy*-90°specimens and the *z*-direction for the *xz*-90° specimens, they have 30% and 10% of fibre orientation, respectively (Fig. 7). It is also interesting that specimens printed at 67.5° and 45° in the *xz*- and *yz*-planes have nearly the same Young's moduli, whereas Young's modulus of *xz*-22.5° are 25% higher than of corresponding *yz*-specimens (Fig. 10). These results indicate that the stiffening effect of the preferable fibre orientation along the *x*-axis is only efficient up to the 45° alignment of the specimens. For the higher specimen alignment angles, however, there is still a small stiffening effect compared to the neat specimens, but to a much smaller extent.

3.3. Optical analysis

3.3.1. Powder

The morphology of the powder particles used to manufacture the specimens is presented in Fig. 11 (both, neat and carbon reinforced powder samples were taken from remaining powder after the processing of the tensile bars). The polyamide particles had a spherical and slightly elongated shape and a rough, porous surface. The typical particle size in Fig. 11 estimated by means of ImageJ is between 30 and 65 μm. The size of porous voids did not exceed 5 μm (Fig. 11b). The fibre lengths estimated in Fig. 11c vary between 50 μm and 250 μm.

3.3.2. Neat specimens

The micrographs of neat specimens, namely *xz*-0° (a, a′) and *xz*-90° (b, b′) are demonstrated in Fig. 12. On the fracture surface of the *xz*-0° specimens, which were printed horizontally along the *x*-axis, the typical SLS layer structure is visible (Fig. 12a). This is not the case for the *xz*-90° specimens, which were printed vertically along the *z*-axis (Fig. 12b). This is because the tensile loads were applied parallel and transverse to the deposited powder layers, respectively. Due to the layer-by-layer manufacturing manner of the SLS process, both the face and side surfaces of *xz*-90° had the layer structure, which is called the staircase effect [44], while *xz*-0° only had it on the side surface. The measured thickness of one fused layer was about 150 μm, which corresponds to the recommendation of the layer thickness to be at least two times the average particle size [3]. The face surface of the horizontally oriented

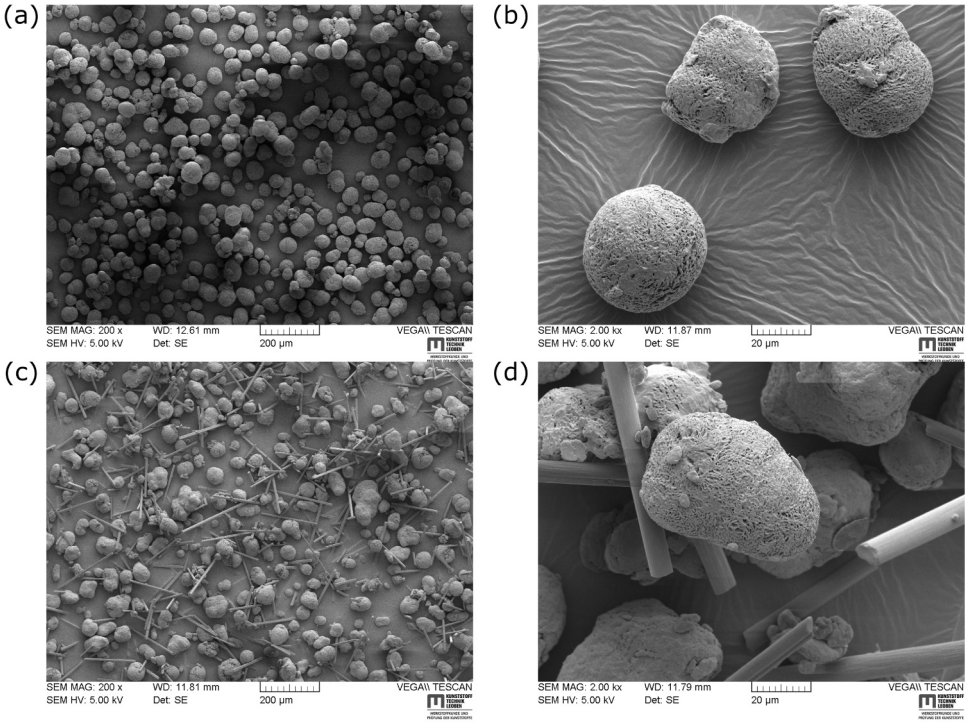

Fig. 11. SEM micrographs of the neat (a, b) and carbon fibre reinforced (c, d) powders used for sintering at low (a, c) and high (b, d) magnification.

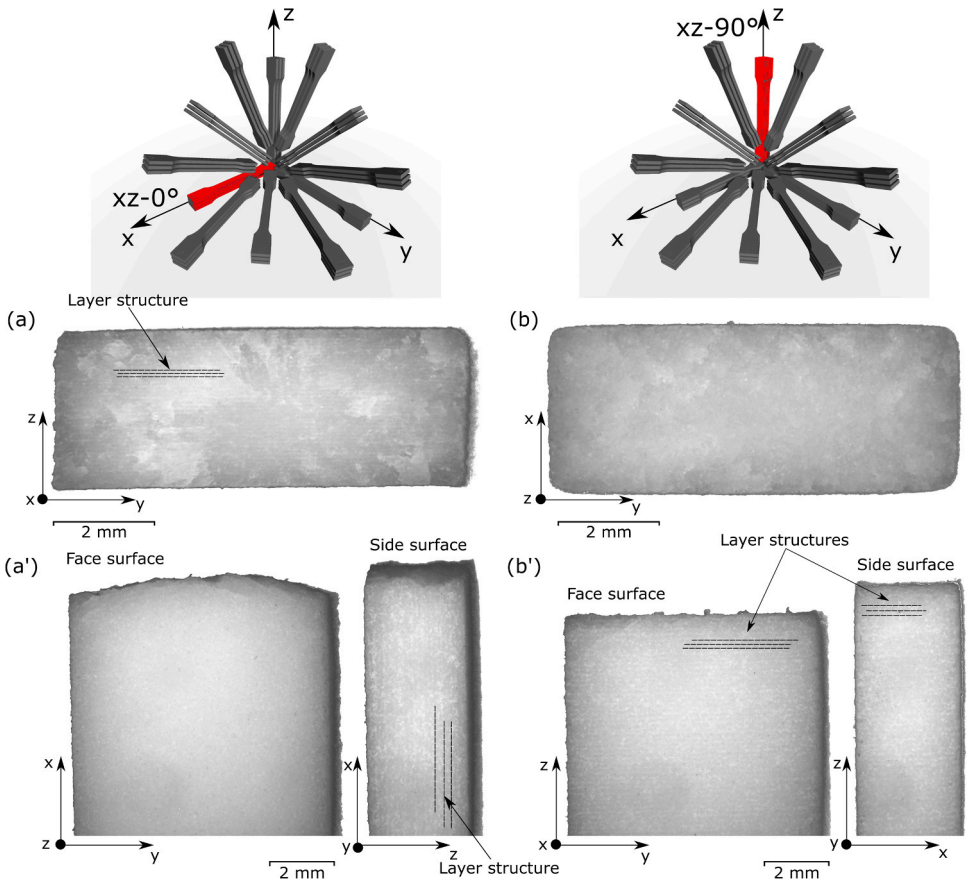

Fig. 12. Fracture surfaces of the *xz*-0° (a) and *xz*-90° (b) neat specimens and the face and side views of their fracture edges (a′, b′).

specimens had a plane and grainy texture, representing the typical surface structure along fused layers.

Correspondingly, the SEM micrographs of *xz*-0° and *xz*-90° are reported in Fig. 13. The images show that a lot of powder particles can be identified either in their full shape or at least their contour on the fracture surface of the *xz*-90° specimen (Fig. 13b). In this regard, the fracture surface of the *xz*-0° specimen has a more compact structure without the obvious presence of powder particles (Fig. 13a). This illustrates well the difference in the loading direction with respect to the printed layer structure: in case of the *xz*-0° alignment, the specimen was loaded parallel to the layer structure, while for the *xz*-90° specimen, the load was applied transverse to it. This means that there was the weaker interlayer adhesion and the higher void concentration in the interfaces between the layers in the latter case [40,45]. The interlayer voids are well illustrated in Fig. 13a. They had round and oblong shapes and sizes from 5 to 100 μm. However, some voids are also visible in Fig. 13b. A further difference between *xz*-0° and *xz*-90° is that in Fig. 13a, a fracture initiation region with corresponding hackle lines [46] can be identified. Such a structure was not found on the *xz*-90° fracture surface (Fig. 13b). This further supports the impression of a more compact fracture surface in the case of the *xz*-0° specimen. In analogy to Fig. 12a′ and Fig. 12b′, the face and side surfaces of the specimens were also studied using SEM. Aside from the above-mentioned variation in the staircase structure, no differences were observed, neither between the front and side surfaces nor between the different printing directions. In all cases, the surfaces were rather homogenous on the macroscopic scale, but inhomogeneous on the microscopic scale. They showed sections with well combined material (molten), areas with clear powder particle contours (unmolten) as well as all intermediate steps in between.

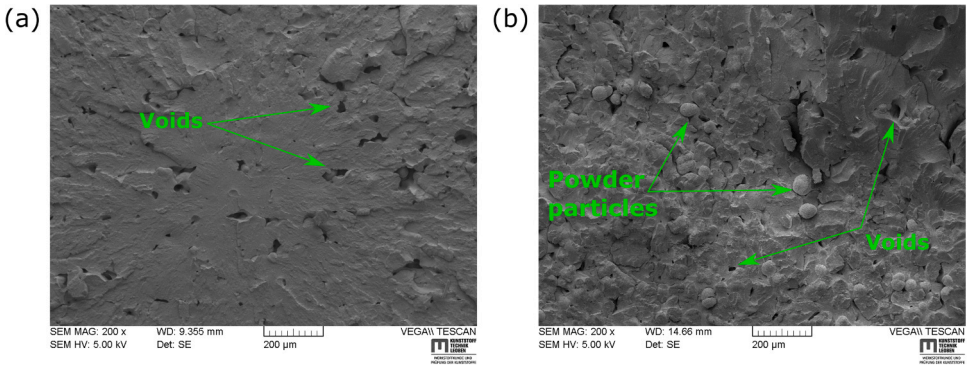

Fig. 13. SEM micrographs of the fracture surfaces of the *xz*-0° (a) and *xz*-90° (b) specimens.

3.3.3. Reinforced specimens

The micrographs of the CF reinforced specimens made with the optical microscope are presented in Fig. 14 for *xz*-0° (a,a,a''), *xz*-45° (b,b′, b′′) and *xz*-90° (c,c′,c′′). The layer structure can be observed on the side surface of *xz*-0° (Fig. 14a′) and the face and side surfaces of *xz*-45° (Fig. 14b′) and *xz*-90° (Fig. 14c′). For *xz*-45° the layer lines were tilted at around 45° on the side surface, which corresponded to the building direction of the specimen (Fig. 14b′). The fracture in the *xz*-90° specimen occurred between the adjacent layers, which is identified by nearly straight fracture edges in Fig. 14c′. This is similar to the fracture surface characteristics of the neat *xz*-90° specimen in Fig. 12b′ and can be explained by the weaker interlayer adhesion and the higher concentration of porosity between the layers [40,45], which indicates that there was no significant fibre reinforcing effect for *xz*-90°. Thus, the SLS layer structure of the matrix dominates the fracture behaviour in this case. The same was observed for the neat specimens. This agrees with the μCT results in Fig. 7 (only small fibre orientation along z-axis) and the tensile test results in Table 3. For the *xz*-45° specimens, the fracture surfaces are tilted with respect to the *xz*-0° and *xz*-90° fracture surface planes. The surfaces are tilted along the thickness with a rotation angle smaller than 45°, as shown in Fig. 14b′. Additionally, the fracture surface of the *xz*-45° specimens demonstrate grooves of the material, which are aligned at about 45° on the surface (Fig. 14b). Tilted fracture surfaces were also noticed for the *yz*-45° and *xy*-45° specimens. In the latter case, the difference was that the tilt was along the width instead of the thickness (rotation angle was also below 45°). Such tilted fracture surfaces are typical for fibre reinforced polymers with preferred fibre orientations not parallel or normal to the load direction [47–50]. Consequently, this effect was also found for the reinforced specimens printed in the 22.5° and 67.5° directions, but not for the corresponding neat specimens. It indicates that the fibre reinforcement dominates the fracture behaviour in these cases instead of the SLS layer structure of the matrix. For the *xz*-0° printing direction, the reinforced specimens show a rather unspecific fracture surface with wavy fracture edges, which was also observed for the neat specimens. Despite these unspecific fracture surfaces, it is clear from the μCT results (Fig. 7) and the tensile test results (Table 3) that the carbon fibre reinforcement dominated the fracture behaviour in the *xz*-0° direction. The higher magnified images of the side surface give a rough picture about the fibre orientations on the specimen surface (Fig. 14a′′–c′′). A more detailed examination on this

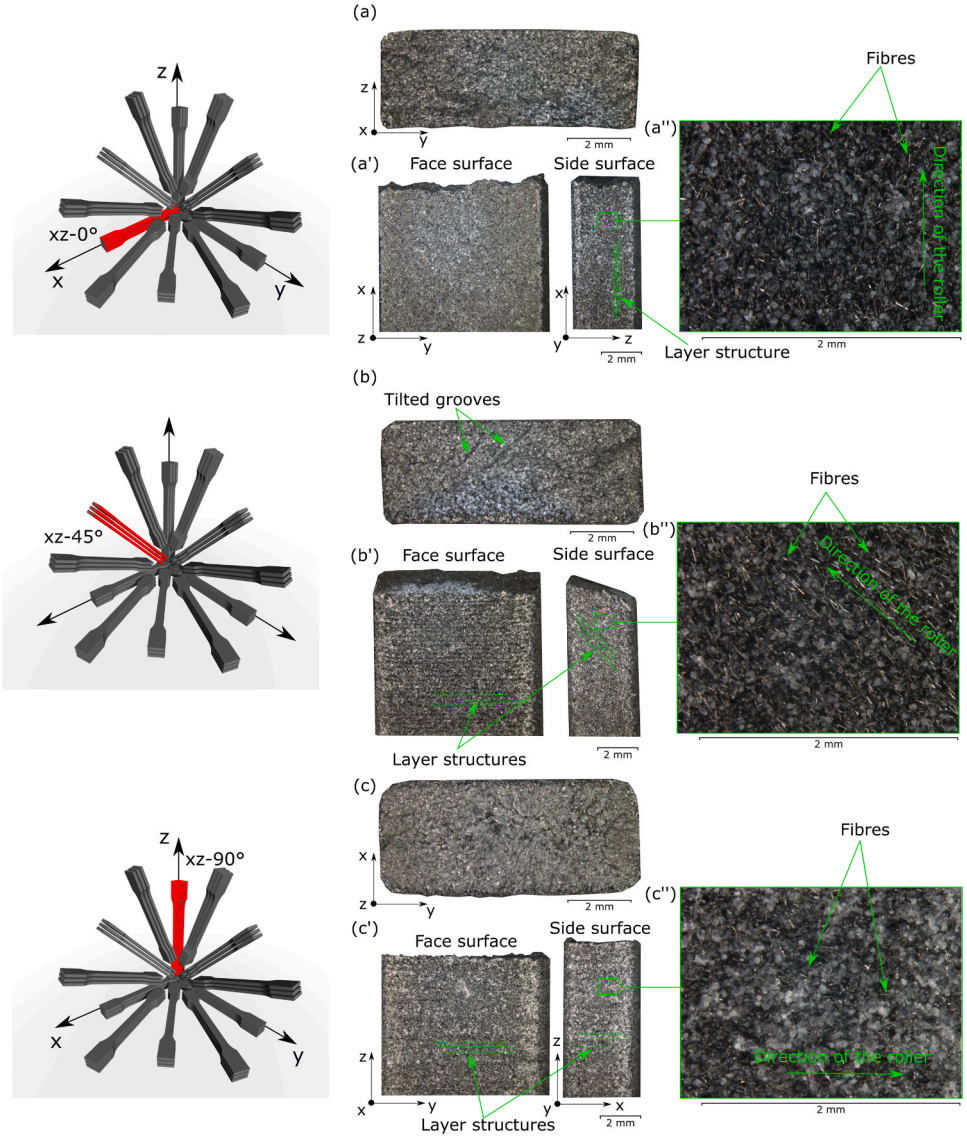

Fig. 14. Fracture surfaces of the *xz*-0° (a), *xz*-45° (b) and *xz*-90° (c) carbon fibre reinforced specimens, their fracture edges (a', b', c') and micrographs of the corresponding side surfaces (a'', b'', c''). The corresponding specimen positions are marked in red on the left side of the figure. (For interpretation of the references to colour in this figure legend, the reader is referred to the web version of this article.)

was performed using SEM.

Fig. 15 shows SEM micrographs of the side surfaces of the *xz*-0° (a), *xz*-45° (b) and *xz*-90°(c) specimens, respectively. Only partly molten powder particles, which are typical for the surfaces of SLS printed parts and were also discussed for the neat specimens, with inclusions of the carbon fibres, can be easily distinguished on the side surfaces of the specimens (Fig. 15a–c). Contrary to that, the fracture surfaces have a rather homogeneous matrix appearance (Fig. 15a′–c′). This phenomenon can be explained by the fact that the laser sintering causes elevated temperatures around the fused area, which yield melting of the loose powder in the immediate vicinity of it [2]. It can be seen that most of the fibres are oriented in the moving direction of the roller, as it is suggested by the μCT results. The presence of the preferable fibre orientation can be also seen in the micrographs of the specimens' fracture surfaces (Fig. 15a′–c′). In *xz*-0°, the fibres stuck out of the matrix almost straight (Fig. 15a′), while in *xz*-45°, the fibres went out of the matrix more tilted (Fig. 15b′). In the case of *xz*-90° (built in *z*-direction), the fibres lay horizontally in the plane of the fracture surface (Fig. 15c′). The micrograph of the fracture surface of *xz*-0° made with the higher magnification demonstrated multiple dark holes in the matrix with a diameter of a fibre (Fig. 15a′). They appeared due to the pulling of fibres out of the matrix as a result of the failure process. The presence of this effect almost faded in *xz*-45° (Fig. 15b′, less dark holes) and disappeared in *xz*-90° (Fig. 15c′, almost no dark holes), which means the load applied was mostly borne by the matrix. These findings are in excellent agreement with the experimental tensile data, where *xz*-0° were the strongest specimens with the highest Young's modulus in comparison with the other building directions.

In Fig. 16, less magnified images of the specimen fracture surfaces are presented to deepen the discussion of the fracture surface characteristics started above. The images belong to three specimens, each of them printed along another main coordinate axis in the building chamber (*x*-axis: *xz*-0°, *y*-axis: *xy*-90° and *z*-axis: *xz*-90°). Regarding the fibre characteristics on the fracture surfaces, the observations from Fig. 15 are also visible on these bigger length scales. For *xz*-0°, these are fibres coming out of the fracture surface perpendicularly and significant fibre pull-out indicated by numerous black holes on the fracture surfaces, which are in the dimension of the fibre diameter (Fig. 16a,a′). For *xz*-90° (Fig. 16c,c′), the absence of these holes and the presence of in-plane fibres instead of out-of-plane fibres was also discussed above. Interestingly, in the *xy*-90° direction (Fig. 16b,b′), the fibre pull-out holes can be clearly identified and their number is not significantly smaller than for the *xz*-0° specimen (Fig. 16a,a′). However, a preferable orientation of the fibres along the roller direction (*x*-axis) can be clearly identified, while for the *xz*-0° specimen, the fibres were oriented mainly perpendicular to the fracture surface.

Looking at the global appearance of the fracture surfaces in Fig. 16, all samples show a brittle-like surface structure with a rocky texture. For *xz*-0° (Fig. 16a,a′), this texture is very rough with fine topographical details on the surface. This printing direction shows the roughest texture

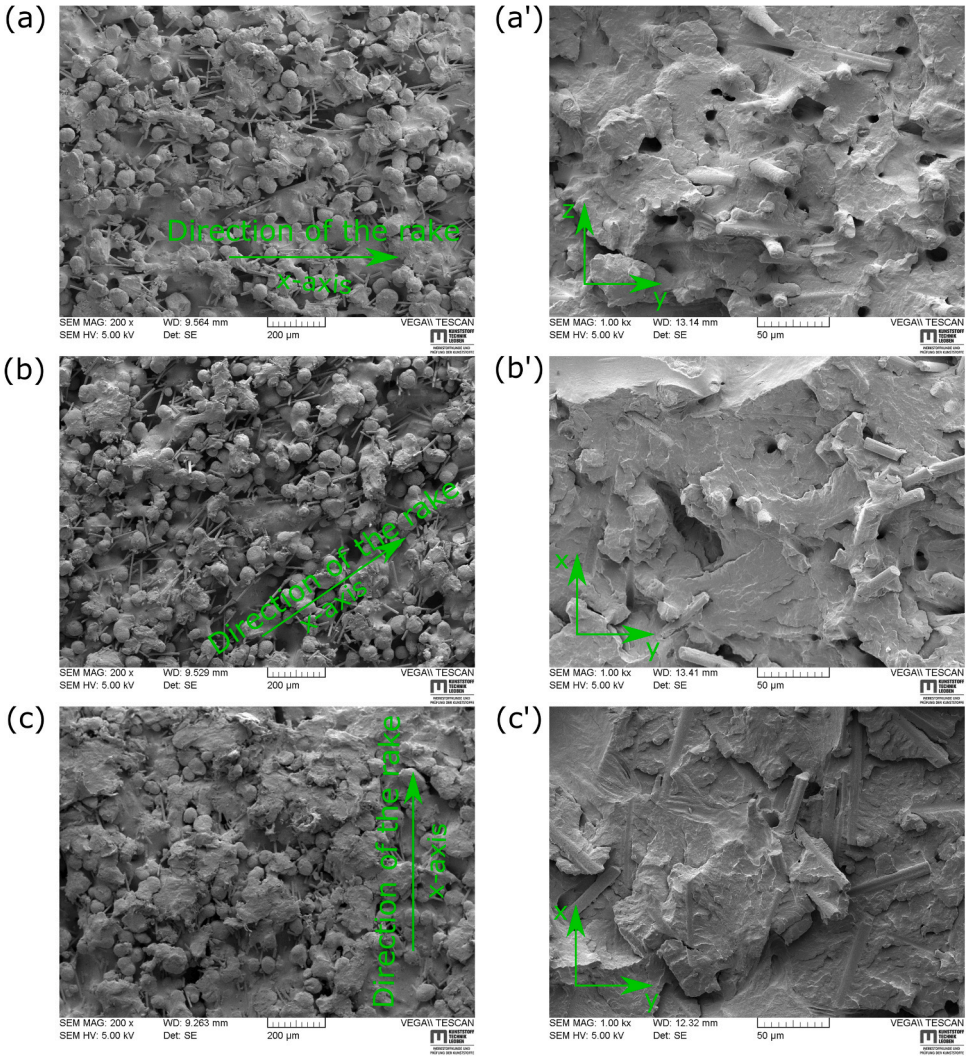

Fig. 15. SEM images of the side (a,b,c) and fracture surfaces (a′,b′,c′) of the *xz*-0°, *xz*-45° and *xz*-90° specimens, respectively.

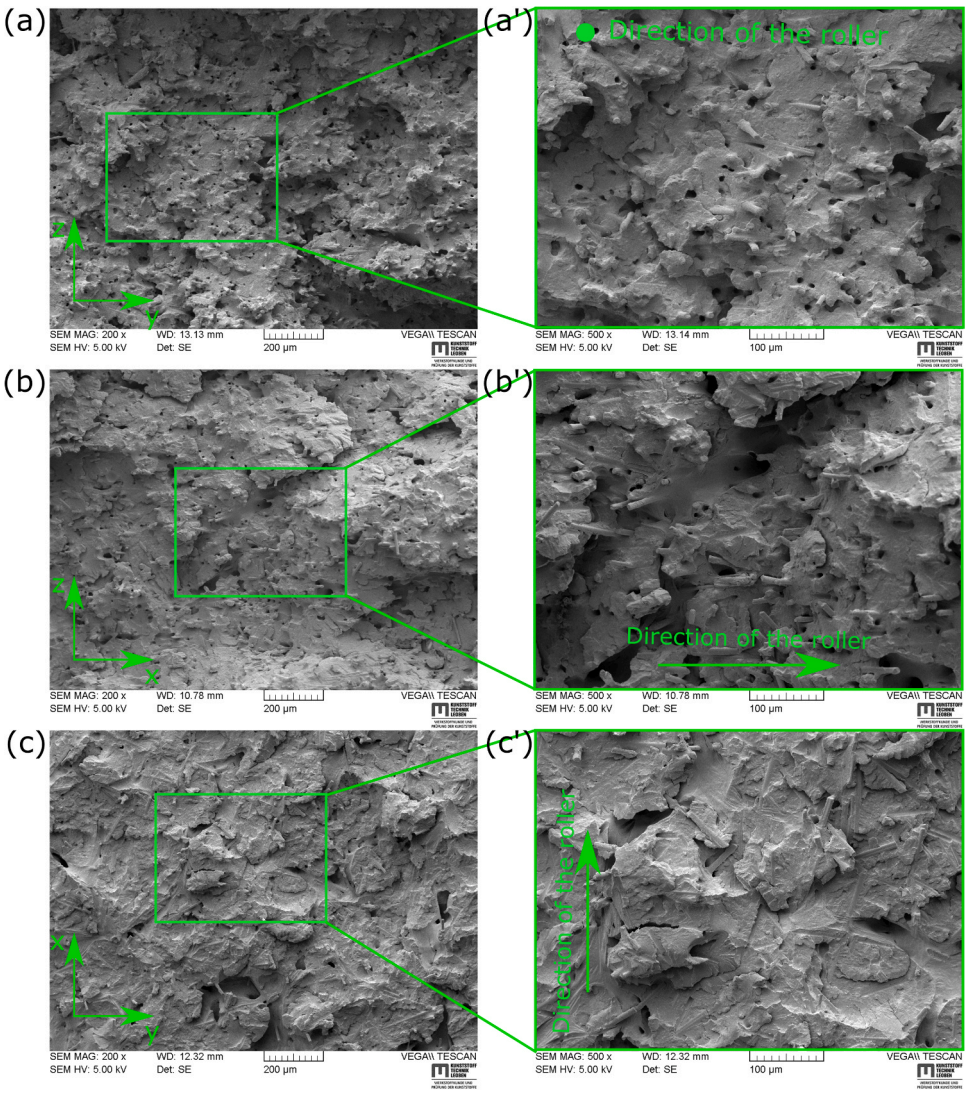

Fig. 16. SEM micrographs of the fracture surfaces of the *xz*-0° (a), *xy*-90° (b) and *xz*-90° (c) specimens.

of all printing directions. The fracture surface texture observed for the *xy*-90° specimen (Fig. 16b,b′) is also rough, but with fewer fine topographical surface details, and hence smoother than that of the *xz*-0° specimen. A global fracture surface texture similar to the latter was found for most of the printing directions. Finally, the fracture surface of the *xz*-90° specimen (Fig. 16c,c′) is rather flat and significantly smoother than the surfaces of all other printing directions. However, it still shows a distinct rocky texture. Moreover, for the *xz*-90° fracture surface, small local areas with a very smooth surface can be identified. Since, in this printing direction, the specimens roughly broke along the SLS layer boundaries (Fig. 14c′), it is interpreted that these local areas represent the surface of interlayer voids. This also explains their smooth melt-like surface. The hypothesis is supported by some remaining voids visible in Fig. 16c,c′, which partly have a connection to these smooth areas. These small void remains were also found on fracture surfaces of other printing directions but to a lesser extent than for *xz*-90°. Based on the images shown in this study and the fracture surface analysis of the further printing directions, it is concluded that the global fracture surfaces of the *xz*-0° and *xz*-90° specimens represent the two extremal values. For all other printing directions, the fracture surfaces can roughly be reduced to a mixture of these two with different mixing ratios.

Hence, recapitulating the discussion above, for the specimens examined in this study, the fibre reinforcement and the fibre orientation introduced by the SLS process were much more important for the mechanical and fracture behaviour than the typical SLS layer structure of the matrix. The only exception is the specimens printed in the *xz*-90° direction, which showed matrix-dominated fracture behaviour.

4. Conclusion

This paper presents the systematic and comprehensive analysis of the mechanical properties of neat and short carbon fibre reinforced polyamide specimens produced by selective laser sintering. The specimens were printed in different directions and different spatial positions in the build chamber. The mechanical parameters, namely tensile strength, Young's modulus and strain at break, were characterised by tensile tests and analysed with respect to these specimen alignments.

The experiments showed a significant influence of the carbon fibres on the material behaviour in the different printing directions. The strength of the reinforced specimens built along the *x*-axis was increased by almost a factor of two, while the strength of the specimens built in the *y*-direction was increased by a factor of nearly 1.4 in comparison with the neat specimens. For the reinforced specimens, the tensile strength and Young's modulus decreased with increasing deviation from the *x*-axis (direction of the powder distribution roller) and with increasing *z*-axis components (manufacturing normal to the layer structure). These findings indicated the existence of a preferable fibre orientation created in the specimens. Detailed investigations with an optical microscope,

scanning electron microscope and X-ray computed tomography showed that the fibres were mainly oriented in-plane of the powder layer in the SLS process and here, especially along the moving direction of the roller. The ratios of the fibre orientation tensor were found as:

- 50 – 60% along the x-axis, which was the roller direction (in-plane of the SLS powder layer)
- 30 – 40% along the y-axis, in-plane perpendicular to the roller direction
- 5 – 15% along the z-axis, normal to the SLS layer structure (out-of-plane fibre orientation)

The μCT analysis showed that the different building alignments did not have an influence on the fibre length distribution. This further strengthened the finding that the change in the mechanical properties was dominated by the fibre orientations. It is worth noting that the μCT analysis was performed using two different software tools. The orientation tensor obtained by extracting individual fibres was in good agreement with the other software based on the grey value orientation analysis. To avoid miss-segmentations of the phase-contrast edge effects along voids, the evaluation of the fibre length was limited to fibres longer than 50 μm for all specimens investigated. The analyses further revealed that the mechanism of the failure changed from 'fibre-matrix' failure for specimens with the fibres oriented along the loading direction to 'matrix-matrix' failure for specimens with the fibres oriented out of the loading direction due to the layer-wise building manner of SLS.

Taken together, the findings obtained highlight the importance of the printing alignment for short fibre reinforced polymer parts produced by SLS. It is clear that the exact values of the above-mentioned fibre orientation ratios in the different machine directions will be dependent on various parameters, such as:

- Type and version of SLS machine
- Powder distribution system: type (roller or blade), size and shape
- Powder characteristics: particle size and shape, packing density, powder ageing state, melt viscosity
- Fibre characteristics: type, size, shape and content
- SLS process parameters: roller speed, powder layer thickness, powder bed temperature, energy density, etc.

Thus the fibre orientation ratios found in this study represent only a single-point result. Nevertheless, they are useful as guide values in component design for the SLS technique. Moreover, they show that through a smart alignment in the building chamber, the SLS process can be used for advanced processing of fibre reinforced components with optimised fibre orientation in essential and critical component parts. However, to fully understand the influence of the above listed parameters on the degree of anisotropy in carbon fibre reinforced specimens produced by SLS, further studies on this topic are required in the future.

CRediT authorship contribution statement

A. Khudiakova: Formal analysis, Investigation, Visualization, Writing - original draft, Writing - review & editing, Validation. **M. Berer**: Conceptualization, Methodology, Resources, Formal analysis, Validation, Writing - original draft, Writing - review & editing, Data curation, Supervision, Project administration. **S. Niedermair**: Conceptualization, Methodology, Resources, Investigation, Formal analysis, Validation. **B. Plank**: Software, Resources, Methodology, Investigation, Formal analysis, Validation, Writing - original draft, Writing - review & editing, Visualization. **E. Truszkiewicz**: Investigation, Formal analysis. **G. Meier**: Investigation. **H. Stepanovsky**: Investigation, Resources. **M. Wolfahrt**: Supervision. **G. Pinter**: Resources, Supervision. **J. Lackner**: Conceptualization, Project administration, Funding acquisition.

Declaration of Competing Interest

The authors declare that they have no known competing financial interests or personal relationships that could have appeared to influence the work reported in this paper.

Acknowledgments

Special thanks go to Nicole Zarfl for the SEM examinations.

The research work of this paper was performed at the Polymer Competence Center Leoben GmbH (PCCL, Austria) within the framework of the funding programs 'Production of the Future', 'Smart Mobility', 'TAKE OFF' and 'COMET-Module' of the Federal Ministry for Transport, Innovation and Technology and the Federal Ministry of Digital and Economic Affairs with contributions by JOANNEUM RESEARCH Forschungsgesellschaft mbH, Institute for Materials Science and Testing of Polymers at the Montanuniversitaet Leoben and Material Center Leoben Forschungs GmbH as Scientific Partners and Rapid Product Development GmbH, LSS GmbH, Bernstein GmbH, Secar Technologie GmbH, F.LIST GmbH, AMES Aerospace and Mechanical Engineering Services, Ing. Walter Starzacher GesmbH, SinusPro GmbH, Inocon Technologie GmbH, Carbon Solutions Hintsteiner GmbH, XeNTiS Entwicklungs- und Produktions GmbH and RÜBIG GmbH & Co KG as company partners. The PCCL is funded by the Austrian Government and the State Governments of Styria, Lower Austria and Upper Austria.

μCT scans and evaluations were performed within the projects 'Interpretation and evaluation of defects in complex CFK structures based on 3D-XCT data and structural simulation - (DigiCT-Sim project number: 862015)' and 'Systematic analysis of three-dimensional pore structures in fibre-reinforced plastics using 3D X-ray methods - (pore3D project number: 868735).' Both μCT projects were funded by the State Government of Upper Austria and Austrian Research Promotion Agency (FFG).

References

[1] University of Texas, Selective Laser Sintering, Birth of an Industry, 2012. ⟨https://www.me.utexas.edu/news/news/selective-laser-sintering-birth-of-an-industry⟩ (Accessed 17 February 2020).
[2] I. Gibson, D. Rosen, B. Stucker. Additive Manufacturing Technologies: 3D Printing, Rapid Prototyping, and Direct Digital Manufacturing, second ed.,, Springer,, New York, NY, 2015.
[3] S. Berretta, O. Ghita, K.E. Evans, Morphology of polymeric powders in Laser Sintering (LS): from polyamide to new PEEK powders, Eur. Polym. J. 59 (2014) 218–229, https://doi.org/10.1016/j.eurpolymj.2014.08.004.
[4] D. Drummer, D. Rietzel, F. Kühnlein, Development of a characterization approach for the sintering behavior of new thermoplastics for selective laser sintering, Phys. Procedia 5 (2010) 533–542, https://doi.org/10.1016/j.phpro.2010.08.081.
[5] J. Bai, B. Zhang, J. Song, G. Bi, P. Wang, J. Wei, The effect of processing conditions on the mechanical properties of polyethylene produced by selective laser sintering, Polym. Test. 52 (2016) 89–93, https://doi.org/10.1016/j.polymertesting.2016.04.004.
[6] P. Chen, H. Wu, W. Zhu, L. Yang, Z. Li, C. Yan, S. Wen, Y. Shi, Investigation into the processability, recyclability and crystalline structure of selective laser sintered Polyamide 6 in comparison with Polyamide 12, Polym. Test. 69 (2018) 366–374, https://doi.org/10.1016/j.polymertesting.2018.05.045.
[7] D. Ritzel, F. Kühnlein, D. Drummer, Selektives Lasersintern von teilkristallinen Thermoplasten, RTejournal Forum Rapid Technol. 6 (2011).
[8] S. Berretta, K.E. Evans, O. Ghita, Processability of PEEK, a new polymer for High Temperature Laser Sintering (HT-LS), Eur. Polym. J. 68 (2015) 243–266, https://doi.org/10.1016/j.eurpolymj.2015.04.003.
[9] W. Zhu, C. Yan, Y. Shi, S. Wen, J. Liu, Y. Shi, Investigation into mechanical and microstructural properties of polypropylene manufactured by selective laser sintering in comparison with injection molding counterparts, Mater. Des. 82 (2015) 37–45, https://doi.org/10.1016/j.matdes.2015.05.043.
[10] R.D. Goodridge, M.L. Shofner, R.J.M. Hague, M. McClelland, M.R. Schlea, R. B. Johnson, C.J. Tuck, Processing of a polyamide-12/carbon nanofibre composite by laser sintering, Polym. Test. 30 (2011) 94–100, https://doi.org/10.1016/j.polymertesting.2010.10.011.
[11] S.R. Athreya, K. Kalaitzidou, S. Das, Processing and characterization of a carbon black-filled electrically conductive nylon-12 nanocomposite produced by selective laser sintering, Mater. Sci. Eng. A 527 (2010) 2637–2642, https://doi.org/10.1016/j.msea.2009.12.028.
[12] S.R. Athreya, K. Kalaitzidou, S. Das, Mechanical and microstructural properties of nylon-12/carbon black composites: selective laser sintering versus melt

compounding and injection molding, Compos. Sci. Technol. 71 (2011) 506–510, https://doi.org/10.1016/j.compscitech.2010.12.028.
[13] A.H. Espera, A. d Valino, J.O. Palaganas, L. Souza, Q. Chen, R.C. Advincula, 3D printing of a robust polyamide-12–carbon black composite via selective laser sintering: thermal and electrical conductivity, Macromol. Mater. Eng. 304 (2019), 1800718, https://doi.org/10.1002/mame.201800718.
[14] J. Bai, R.D. Goodridge, R.J.M. Hague, M. Song, Carbon nanotube reinforced polyamide 12 nanocomposites for laser sintering, in: D.L. Bourell, R.H. Crawford, C.C. Seepersad, J.J. Beaman, H.L. Marcus (Eds.), 23rd Annual International Solid Freeform Fabrication Symposium: An Additive Manufacturing Conference, Proceedings, August 6–8, 2012, University of Texas, 2012, pp. 98–107.
[15] J. Bai, R.D. Goodridge, R.J.M. Hague, M. Song, Improving the mechanical properties of laser-sintered polyamide 12 through incorporation of carbon nanotubes, Polym. Eng. Sci. 53 (2013) 1937–1946, https://doi.org/10.1002/pen.23459.
[16] B. Chen, S. Berretta, K. Evans, K. Smith, O. Ghita, A primary study into graphene/polyether ether ketone (PEEK) nanocomposite for laser sintering, Appl. Surf. Sci. 428 (2018) 1018–1028, https://doi.org/10.1016/j.apsusc.2017.09.226.
[17] H. Chung, S. Das, Processing and properties of glass bead particulate-filled functionally graded nylon-11 composites produced by selective laser sintering, Mater. Sci. Eng. A 437 (2006) 226–234, https://doi.org/10.1016/j.msea.2006.07.112.
[18] W. Jing, C. Hui, W. Qiong, L. Hongbo, L. Zhanjun, Surface modification of carbon fibers and the selective laser sintering of modified carbon fiber/nylon 12 composite powder, Mater. Des. 116 (2017) 253–260, https://doi.org/10.1016/j.matdes.2016.12.037.
[19] A. Jansson, L. Pejryd, Characterisation of carbon fibre-reinforced polyamide manufactured by selective laser sintering, Addit. Manuf. 9 (2016) 7–13, https://doi.org/10.1016/j.addma.2015.12.003.
[20] B. Chen, S. Berretta, R. Davies, O. Ghita, Characterisation of carbon fibre (Cf) - Poly Ether Ketone (PEK) composite powders for laser sintering, Polym. Test. 76 (2019) 65–72, https://doi.org/10.1016/j.polymertesting.2019.03.011.
[21] W. Jing, C. Hui, W. Qiong, L. Hongbo, L. Zhanjun, Surface modification of carbon fibers and the selective laser sintering of modified carbon fiber/nylon 12 composite powder, Mater. Des. 116 (2017) 253–260, https://doi.org/10.1016/j.matdes.2016.12.037.
[22] M. Yan, X. Tian, G. Peng, D. Li, X. Zhang, High temperature rheological behavior and sintering kinetics of CF/PEEK composites during selective laser sintering, Compos. Sci. Technol. 165 (2018) 140–147, https://doi.org/10.1016/j.compscitech.2018.06.023.
[23] G. Flodberg, H. Pettersson, L. Yang, Pore analysis and mechanical performance of selective laser sintered objects, Addit. Manuf. 24 (2018) 307–315, https://doi.org/10.1016/j.addma.2018.10.001.
[24] B. Chen, Y. Wang, S. Berretta, O. Ghita, Poly Aryl Ether Ketones (PAEKs) and carbon-reinforced PAEK powders for laser sintering, J. Mater. Sci. 52 (2017) 6004–6019, https://doi.org/10.1007/s10853-017-0840-0.
[25] W. Zhu, C. Yan, Y. Shi, S. Wen, J. Liu, Q. Wei, Y. Shi, A novel method based on selective laser sintering for preparing high-performance carbon fibres/polyamide12/epoxy ternary composites, Sci. Rep. 6 (2016) 33780, https://doi.org/10.1038/srep33780.
[26] S. Arai, S. Tsunoda, A. Yamaguchi, T. Ougizawa, Effects of short-glass-fiber content on material and part properties of poly(butylene terephthalate) processed by selective laser sintering, Addit. Manuf. 21 (2018) 683–693, https://doi.org/10.1016/j.addma.2018.04.019.
[27] ⟨http://en.farsoon.com/products_detail/productId=41.html⟩ (Accessed April 2020).
[28] ⟨https://www.sglcarbon.com/en/markets-solutions/material/sigrafil-short-carbon-fibers/⟩ (Accessed April 2020).
[29] ISO 527, Plastics - Determination of tensile properties.
[30] D. Salaberger, K.A. Kannappan, J. Kastner, J. Reussner, T. Auinger, Evaluation of computed tomography data from fibre reinforced polymers to determine fibre length distribution, Int. Polym. Process. 26 (2011) 283–291.
[31] Salaberger D., Hine P.J., Jerabek M., Kastner J., Assessment of accuracy of fibre orientation measurement using X-ray computed tomography, in: 20th International Conference on Composite Materials (2015).
[32] github.com/3dct/open_iA (Accessed April 2020).
[33] Kastner J., Plank B., Salaberger D., Sekelja J., Defect and porosity determination of fibre reinforced polymers by X-ray computed tomography, in: 2nd International Symposium on NDT in Aerospace (2010).
[34] S. Senck, M. Scheerer, V. Revol, K. Dobes, B. Plank, J. Kastner, Non-Destructive Evaluation of Defects in Polymer Matrix Composites for Aerospace Applications Using X-ray Talbot-Lau Interferometry and Micro CT., in: AIAA SciTech Forum: 58th AIAA/ASCE/AHS/ASC Structures, Struct. Dyn., Mater. Conf. (2017).
[35] Plank B., Rao G., Kastner J., Evaluation of CFRP-reference samples for porosity made by drilling and comparison with industrial porosity samples by means of quantitative XCT, in: 7th International Symposium on NDT in Aerospace (2015).
[36] Reiter M., Erler M., Kuhn C., Gusenbauer C., Kastner J., SimCT: a simulation tool for X-ray imaging, in: 6th Conference on Industrial Computed Tomography (2016).
[37] D. Salaberger, Micro structure of discontinuous fibre polymer matrix composites determined by X-ray Computed Tomography, Doctoral dissertation (2019).
[38] ISO 22314:2006, Plastics — Glass-fibre-reinforced products — Determination of fibre length.
[39] J. Kastner, B. Plank, G. Requena, Non-destructive characterisation of polymers and Al-alloys by polychromatic cone-beam phase contrast tomography, Mater. Charact. 64 (2012) 79–87, https://doi.org/10.1016/j.matchar.2011.12.004.
[40] E.C. Hofland, I. Baran, D.A. Wismeijer, Correlation of process parameters with mechanical properties of Laser Sintered PA12 parts, Adv. Mater. Sci. Eng. 2017 (2017) 1–11, https://doi.org/10.1155/2017/4953173.
[41] A. Wegner, G. Witt, Correlation of process parameters and part properties in Laser Sintering using response surface modeling, Phys. Procedia 39 (2012) 480–490, https://doi.org/10.1016/j.phpro.2012.10.064.
[42] J.R.C. Dizon, A.H. Espera, Q. Chen, R.C. Advincula, Mechanical characterization of 3D-printed polymers, Addit. Manuf. 20 (2018) 44–67, https://doi.org/10.1016/j.addma.2017.12.002.
[43] C. Soutis, Carbon fiber reinforced plastics in aircraft construction, Mater. Sci. Eng. A 412 (2005) 171–176, https://doi.org/10.1016/j.msea.2005.08.064.
[44] M. Schmid, Laser Sintering with Plastics: Technology, Processes, and Materials, Carl Hanser Verlag, Munich, 2018.
[45] B. Caulfield, P.E. McHugh, S. Lohfeld, Dependence of mechanical properties of polyamide components on build parameters in the SLS process, J. Mater. Process. Technol. 182 (2007) 477–488, https://doi.org/10.1016/j.jmatprotec.2006.09.007.
[46] ASM International, Characterization and Failure Analysis of Plastics, ASM International, Materials Park, OH, 2010.
[47] A. Benaarbia, A. Chrysochoos, G. Robert, Fiber orientation effects on heat source distribution in reinforced polyamide 6.6 subjected to low cycle fatigue, J. Eng. Math. 90 (2015) 13–36, https://doi.org/10.1007/s10665-014-9720-7.
[48] S. Mortazavian, A. Fatemi, Effects of fiber orientation and anisotropy on tensile strength and elastic modulus of short fiber reinforced polymer composites, Compos. Part B Eng. 72 (2015) 116–129, https://doi.org/10.1016/j.compositesb.2014.11.041.
[49] S. Mortazavian, A. Fatemi, Fatigue behavior and modeling of short fiber reinforced polymer composites including anisotropy and temperature effects, Int. J. Fatigue 77 (2015) 12–27, https://doi.org/10.1016/j.ijfatigue.2015.02.020.
[50] K. Tanaka, T. Kitano, N. Egami, Effect of fiber orientation on fatigue crack propagation in short-fiber reinforced plastics, Eng. Fract. Mech. 123 (2014) 44–58, https://doi.org/10.1016/j.engfracmech.2014.03.019.